International Journal of Hydrogen Energy 228 (2026) 154578

Contents lists available at ScienceDirect

International Journal of Hydrogen Energy

journal homepage: www.elsevier.com/locate/he

Activation of powder-coated electrodes for the alkaline oxygen evolution reaction

Christian Marcks [a,*], Clara Gohlke [a], Mohit Chatwani [b], Adarsh Jain [b], Timo Wagner [c], Nicolas Wöhrl [c,d], Vineetha Vinayakumar [b,d], Vera Seidl [a], Doris Segets [b,d], Anna K. Mechler [a,*]

[a] Electrochemical Reaction Engineering (AVT.ERT), RWTH Aachen University, Forckenbeckstraße 51, Aachen, 52074, Germany
[b] Institute for Energy and Materials Processes – Particle Science and Technology (EMPI-PST), University of Duisburg–Essen, Carl-Benz-Straße 199, Duisburg, 47057, Germany
[c] Faculty of Physics, University of Duisburg–Essen, Lotharstr. 1, Duisburg, 47057, Germany
[d] Center for Nanointegration Duisburg–Essen (CENIDE), Carl-Benz-Straße 199, Duisburg, 47057, Germany

ARTICLE INFO

Keywords:
Alkaline water electrolysis
Ball milling
Electrochemical conditioning
Electrochemistry
Plasma treatment

ABSTRACT

To address the challenges of climate change, efficient green hydrogen production via alkaline water electrolysis is essential. Enhanced efficiency can be achieved not only by catalyst design, but also by pre-treatment of the catalyst-coated electrodes. In this study, we transfer previously optimized electrochemical conditioning protocols to spray-coated $NiCoO_2$ anodes and compare their effects with plasma treatment and ball milling. While plasma treatment enhances activity for the oxygen evolution reaction, combining plasma treatment with electrochemical conditioning further improves performance, reducing the potential required to reach 100 mA cm^{-2} by over 50 mV. Plasma treatment also improves catalyst-layer adhesion, reducing delamination during conditioning. However, delamination could not be fully prevented for intensive conditioning protocols involving cycling into the hydrogen evolution regime. Applying these protocols to more mechanically stable electrodes could enable further improvements. Overall, our findings highlight the importance of electrode pretreatment and optimized processing protocols to enhance both activity and stability.

1. Introduction

Hydrogen is a crucial energy carrier, enabling renewable energy storage and replacing fossil fuels in industrial processes, playing a key role in achieving net-zero targets. Alkaline water electrolysis (AWE) is an established process for the production of green hydrogen and requires low-cost, highly efficient and stable electrocatalysts for the oxygen evolution reaction (OER). Ni-,Fe-, and Co-based materials have been widely studied as highly active OER catalysts [1–9]. Among them, Ni–Fe-based catalysts exhibit excellent activity, and are widely adopted in alkaline water electrolysis systems. However, iron dissolution during operation creates challenges for electrolyzer designs that employ high-performing cathodes. While dissolved iron enhances OER activity on Ni anodes, it simultaneously deactivates noble metal-based cathodes [10]. As electrolyzer manufactures consider pairing Ni-based anodes with noble-metal cathodes, Fe-free systems remain an industrially relevant alternative [10,11]. In this work we, therefore, focus on Fe-free Ni–Co-based electrocatalysts and investigate how different pre-treatment methods influence their properties.

Beyond their intrinsic performance, a catalyst's activity is largely determined by its structural properties such as particle size distribution and the resulting layer homogeneity and microstructure as well as its surface oxidation state [12–14]. These properties can be tailored through synthesis and pre-treatment — both chemically and electrochemically. The synthesis of Ni–Co-based catalysts for the alkaline OER can involve various methods to achieve desired morphologies and structures. For example, electrodeposition enables controlled growth of Ni–Co-alloys with specific morphologies, such as nanowires or nanocrystals [15,16]. Alternatively, metal–organic frameworks serve as precursors that can be transformed into nanosheets or porous Ni–Co-nitrides upon annealing in an NH_3 atmosphere [17]. Spray coating of nanoparticles such as NiO, Co_3O_4 and $NiCo_2O_4$ provides another route to form thin film electrocatalysts [18,19]. To enhance OER performance and increase catalyst stability, several treatment techniques are applied, including surface nitridation, which increases active sites and facilitates electron transfer, as well as the integration of conductive substrates

* Corresponding authors.
E-mail addresses: christian.marcks@avt.rwth-aachen.de (C. Marcks), anna.mechler@avt.rwth-aachen.de (A.K. Mechler).

https://doi.org/10.1016/j.ijhydene.2026.154578
Received 14 January 2026; Received in revised form 13 March 2026; Accepted 16 March 2026
Available online 24 March 2026

like carbon cloth or graphene [20–22]. Annealing, calcination and electrochemical treatments of the synthesized layers are often employed subsequently to the deposition or coating of the materials, further increasing the catalytic activity [19,23,24].

However, despite the fact that pre-treatment seemingly plays a crucial role in catalyst activation, its effects and best practices are not fully understood, yet. In this study, we utilize and combine different pre-treatment methods to tune the activity as well as to improve the adhesion of particle-based catalyst layers: (a) electrochemical conditioning, (b) ball milling of catalyst powder, and (c) plasma treatment of catalyst layers [14,25–27].

Electrochemical conditioning, typically by cyclic voltammetry (CV), is a common experimental step prior to the actual catalysts activity determination not only for OER but also for other catalytic processes, such as the oxygen reduction reaction (ORR) and the hydrogen evolution reaction (HER) [28–31]. The conditioning is primarily used to oxidize and remove surface impurities while ensuring the electrocatalyst's surface reaches its active state prior to further experiments. In a previous work, we systematically investigated the impact of CV-conditioning on a $Ni_{70}Fe_{30}$ bulk electrode in an electrochemical flow cell (EFC) [14]. We demonstrated that CV-conditioning leads to an activation, which is strongly influenced by the applied potential window, scan rate, and the number of cycles. Furthermore, improved activation for larger potential windows, i.e., conditioning into OER and HER potentials, a low scan rate, and a high number of cycles were found. For fixed conditioning times, a high scan rate is beneficial. Optimized conditions, such as cycling between $-0.35 - 1.6$ V vs. RHE at $100\,mV\,s^{-1}$ for 30 min, resulted in a significant reduction of the OER overpotential by 47 ± 6 mV at $10\,mA\,cm^{-2}$. The observed enhancement was attributed to the growth of a hydrous oxide layer, while Fe incorporation or dissolution played only a minor role.

While ball milling is commonly used to reduce catalyst particle size, we showed in another study that it can also induce significant structural modifications that impact the intrinsic catalytic performance [25]. The oxide materials undergo phase transformations, which directly influence their electrochemical activity. In this previous study, ball milled $NiCoO_2$ exhibited the highest OER activity, reaching a mean potential of 1.56 V vs. RHE at $10\,mA\,cm^{-2}$, compared to 1.61 V vs. RHE, without any treatment. This improved performance is attributed to an initial $Ni(OH)_2$ reduction as well as particle fragmentation, highlighting the benefits of controlled structural modification via ball milling. The findings emphasize that, beyond particle size reduction, ball milling can serve as a pre-treatment strategy to enhance catalytic properties by tuning the phase composition.

Plasma treatment is another promising surface modification technique that alters catalyst morphology and composition. This method involves exposing catalyst materials to a plasma environment, which can induce significant modifications in their surface properties, thereby enhancing their catalytic performance. For instance, Xu et al. [26] demonstrated that an argon plasma treatment of Co_3O_4 nanosheets not only increased their surface area but also generated oxygen vacancies, leading to a higher Co^{2+}/Co^{3+} ratio. These changes resulted in a substantial improvement in OER activity, with the plasma-engraved Co_3O_4 exhibiting a much higher current density and a lower onset potential compared to the pristine material. Similarly, Le et al. [32] reported that nitrogen plasma treatment of a Ni–Co-based catalyst induced oxygen vacancies and nitrogen doping in the catalyst structure. These modifications considerably improved the charge transfer efficiency, which results in excellent OER performance in alkaline media with a low overpotential of 289 mV at $10\,mA\,cm^{-2}$ and high stability over 24 h. Wagner et al. [33] further showed that plasma treatment of nickel surfaces can increase the specific surface area by introducing a porous network of nickel nitrides. Furthermore, the treatment removes necessary binder for coatings and can reduce the OER overpotential by ≈ 46 mV at $100\,mA\,cm^{-2}$ [27]. All studies underscore the potential of plasma treatment as an effective pre-treatment strategy to tailor the surface characteristics of catalysts, thereby optimizing their activity and stability for the OER.

While each of these pre-treatment strategies has been shown to influence catalyst performance, their transferability to conventional powder-based thin-film electrodes and their combined application have not yet been investigated. In particular, it remains unclear whether electrochemical conditioning procedures developed for bulk electrodes can be directly applied to thin-film electrodes.

In this work, we therefore investigate commercial nickel cobalt oxide ($NiCoO_2$) powder catalysts deposited as thin-film electrodes by ultrasonic spray coating. First, electrochemical conditioning procedures previously established by Gohlke et al. [14] for $Ni_{70}Fe_{30}$ bulk electrodes in an EFC are adapted to a beaker cell setup and evaluated for their transferability to the Ni–Co catalyst system. Subsequently, additional pre-treatment strategies, namely ball milling of the catalyst powder and plasma treatment of the deposited catalyst layers, are investigated to improve the structural integrity and to achieve further enhancements in combination with electrochemical conditioning. The resulting data is correlated to surface changes, characterized by optical microscopy, scanning electron microscopy (SEM), energy dispersive X-ray spectroscopy (EDX), and X-ray photoelectron spectroscopy (XPS).

2. Experimental

2.1. Electrochemical procedures

The fabricated layers were employed as working electrodes (WE) in three-electrode beaker cell and flow cell setups (see Figure S1). The beaker cell setup is a modified version of the cell presented by Thissen et al. [34], adapted for plate electrodes as described by Jain et al. [12]. A detailed description of the EFC is provided elsewhere [14]. The experimental setup and measurement procedures closely follow those reported by Jain et al. [12] and are described in detail in the Supplementary Information (SI), sections S2 and S3. Two experimental protocols were employed: (i) a primary activity determination (PAD) protocol to assess electrode activity and short-term stability, and (ii) an electrochemical conditioning protocol.

2.1.1. Primary activity determination protocol

In short, the PAD protocol comprises three steps. First, the initial electrode activity is determined. This is followed by a stability test consisting of four consecutive cycles, with the central step being a chronopotentiometry (CP) measurement at $100\,mA\,cm^{-2}$. The protocol concludes with a second activity determination performed under conditions similar to those of the initial measurement.

2.1.2. Electrochemical conditioning

The electrochemical conditioning protocols are similar to those presented by Gohlke et al. [14] The protocols contain one CP activity determination step prior and one after the conditioning step ($\overline{E}_{i,\mathrm{before}}$ and $\overline{E}_{i,\mathrm{after}}$). The respective potentials are averaged by calculating the mean value over the CPs final 120 s. As a measure for the activation of the electrodes, the potential difference ΔE_i, at a given current density i, is calculated according to Eq. (1):

$$\Delta E_i = \overline{E}_{i,\mathrm{after}} - \overline{E}_{i,\mathrm{before}} \tag{1}$$

Conditioning was performed by CV with three different sequences: SEQ01 ($-0.35 - 1.6$ V vs. RHE, $10\,mV\,s^{-1}$), SEQ02 ($-0.35 - 1.6$ V vs. RHE, $100\,mV\,s^{-1}$) and SEQ03 ($0.5 - 1.6$ V vs. RHE, $10\,mV\,s^{-1}$). If not further specified, 300 cycles were performed in each sequence. Further details of the protocol are shown in Figure S3 and Table S2

2.2. Layer fabrication

2.2.1. Ball milling

The commercial $NiCoO_2$ catalyst (99 %, CAS: 58591-45-0, Sigma-Aldrich) was subjected to planetary ball milling (PM-100, Retsch) at

a constant weight ratio of $NiCoO_2$ to zirconium oxide beads (1 mm diameter) of 1:150 [35]. Prior to milling, milli-Q water was added at a rate of 2 mg μL^{-1} (based on the catalyst mass). The mill was operated at 400 rpm for a total of 2 h with a 1 min cooling interval between milling cycles to mitigate thermal effects. In addition, the rotation direction was alternated between clockwise and anticlockwise every 30 min to promote homogeneous grinding. Following the milling procedure, the resulting product was retrieved via milli-Q water flushing and subsequently dried in a vacuum oven at 60 °C for 20 h to ensure complete removal of residual moisture.

2.2.2. Ink formulation

Catalyst inks were prepared following established procedures from our previous work [12,27]. Briefly, the catalyst powder was dispersed at a concentration of 1 mg mL^{-1} in a 50:50 wt.% water–ethanol mixture. The suspension was tip-sonicated for a total of 18 min, with the binder added during the final 6 min. Sonication was performed under ice-bath cooling to suppress heating and re-agglomeration, while the ink stability was assessed by analytical centrifugation. More information about the ink formulation process is given in SI, section S4.

2.2.3. Coating

Coatings were performed as described in our previous work [12]. A detailed description is given in the SI, section S5. Briefly, the inks were deposited onto nickel plates (99.2 %, 1 cm^2) using an ultrasonic spray coater. 80 layers of the inks were sprayed at 0.4 mL min^{-1}, achieving mass loadings of approximately 450 μg cm^{-2}.

2.2.4. Plasma treatment

We refer to our previous work [27] for the plasma treatment, as the exact same protocol was applied to these samples. In short, the deposited layers were treated in a custom build microwave plasma reactor under nitrogen atmosphere. The plasma was ignited at a microwave power of 1 kW and applied for 10 min with the sample positioned on a glass holder.

2.3. Characterization

SEM, EDX & XPS were performed similar to the work by Jain et al. [12] and are detailed again in the SI, section S6. In summary, SEM & EDX were carried out using a Hitachi TM3030 tabletop SEM equipped with a Quantax70 EDX detector. For EDX analysis, three locations per sample were evaluated, excluding regions with evident catalyst detachment.

XPS was conducted using a near-ambient-pressure system with a monochromated Al-Kα source (1486.6 eV). Survey spectra were acquired at a pass energy of 100 eV, followed by high-resolution scans of Ni, Co, and O at 20 eV and a resolution of 0.05 eV.

3. Results and discussion

3.1. Transferability

Based on the experimental procedure developed by Gohlke et al. [14] for an EFC setup with $Ni_{70}Fe_{30}$ bulk electrodes, we investigated its transferability to a beaker cell configuration (setups are displayed in Figure S1). This modification is necessary because incorporating powder-based electrodes into the EFC setup would result in significant material waste, as each sample would need to be embedded in epoxy resin. The goal is to gradually mimic the stagnant and batch conditions of a beaker cell by transitioning from a single-pass flow to a circular flow. Subsequently, the flow rate is reduced from 3 mL min^{-1} to the lowest feasible rate in the EFC, 0.9 mL min^{-1}, where the convective mass transport remains sufficient to efficiently remove evolving gas bubbles. Fig. 1 shows the activation behavior for the subsequent steps of the transfer from the EFC to the beaker cell, as well as the replication of

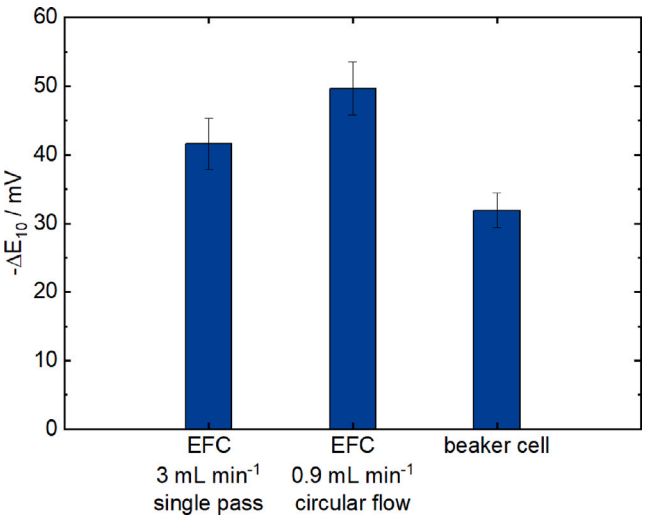

Fig. 1. Comparison of the activation of $Ni_{70}Fe_{30}$ in the EFC and the beaker cell employed in this work. Conditioning settings were −0.35 – 1.6 V vs. RHE, 100 mV s^{-1}, 46 cycles, RT, 1 M KOH.

the activation behavior reported by Gohlke et al. [14] (the respective conditioning CVs are shown in Figure S4). While the reduction of the flow rate or switching to a circular flow has no significant impact on electrode activation, in the beaker cell setup, activation decreased from 50 ± 4 mV to 32 ± 3 mV. One possible explanation could lie in the actual electrode surface area. In the EFC, the geometric surface area of the electrodes is exactly defined as 1 cm^2, since the electrode is embedded in an epoxy polymer, exposing only one surface to the electrolyte. In contrast, in the beaker cell, the electrode holder partially covers the electrode (approximately 13 %), reducing the actual surface area in contact with the electrolyte. On the other hand, the sides of the cuboid-shaped 1 cm^2 plate electrodes are exposed to the electrolyte, potentially increasing the active surface area. This effect can be significant, as the sides could add up to approximately 0.3 cm^2 to the assumed surface area of 1 cm^2.

This is supported by the higher activity of electrodes measured in the beaker cell even before conditioning (see Figure S5). Another key difference between the two systems is the reduced convection in the beaker cell, which is achieved by stirring with a magnetic stirrer at 100 rpm. Compared to the EFC, gas bubbles may not be removed as effectively, due to the absence of shear forces introduced by electrolyte flow [36] (gas bubbles on the electrode surface are visualized in Figure S6). This may increase ohmic resistance and reduce the active surface area. Portions of the electrode covered by evolving gas bubbles may not be in contact with the electrolyte, thereby reducing the effectiveness of the conditioning process and leading to lower activation. Nevertheless, a clear activation could still be observed in the beaker cell, and – within experimental error as previously described – remained within the expected range. Thus, pre-treatment by electrochemical conditioning was successfully transferred to the beaker cell configuration and is applicable for studies involving powder-based electrodes.

3.2. Protocol optimization of powder-coated anodes

To optimize the electrochemical conditioning protocol for powder-coated anodes, we investigated the activation behavior of a spray coated $NiCoO_2$ on a Ni99.2 support and compared it to a bulk $Ni_{70}Fe_{30}$ electrode. Fig. 2 shows the activation of both electrodes at 10 mA cm^{-2} after a mild electrochemical conditioning between 0.5 – 1.6 V, at 10 mV s^{-1} (the respective conditioning CVs are given in Figure S7). After

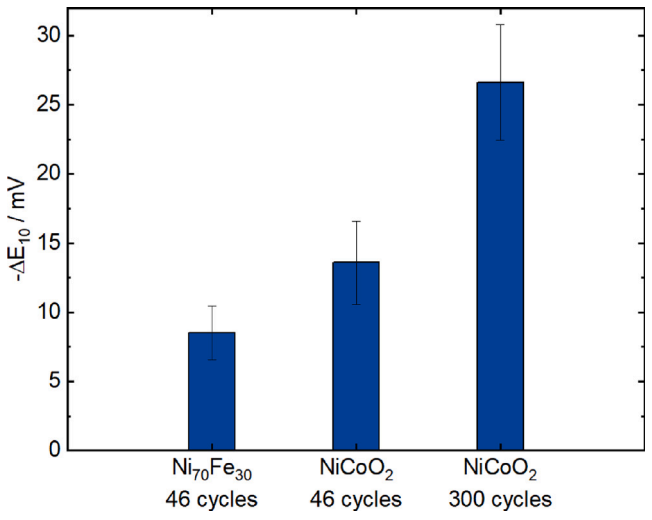

Fig. 2. Activation comparison of $Ni_{70}Fe_{30}$ (46 cycles) and $NiCoO_2$ (46 cycles and 300 cycles). Conditioning was performed in the potential range of 0.5 – 1.6 V vs. RHE with 10 mV s^{-1}.

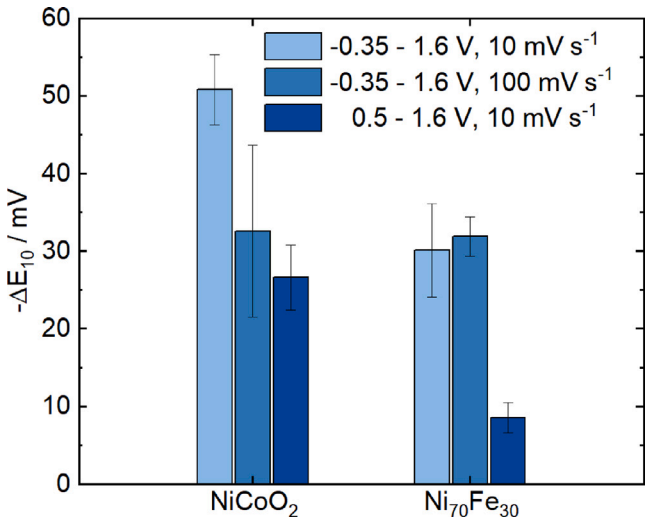

Fig. 3. Activation ($-\Delta E_{10}$) at 10 mA cm^{-2} of $NiCoO_2$ and $Ni_{70}Fe_{30}$ due to conditioning performed in 1 M KOH at RT with SEQ01 (−0.35 – 1.6 V vs. RHE, 10 mV s^{-1}), SEQ02 (−0.35 – 1.6 V vs. RHE, 100 mV s^{-1}) and SEQ03 (0.5 – 1.6 V vs. RHE, 10 mV s^{-1}). Please note that the bulk $Ni_{70}Fe_{30}$ underwent 46 cycles (5 h, 0.5 h and 2.8 h total conditioning time for SEQ01, SEQ02 and SEQ03, respectively) while all powder-coated anodes underwent 300 cycles (32.5 h, 3.25 h and 18.3 h total conditioning time for SEQ01, SEQ02 and SEQ03, respectively). Catalyst loading is ≈450 µg cm^{-2}.

46 conditioning cycles, the $NiCoO_2$ electrode exhibits similar activation values (14 ± 3 mV) compared to the $Ni_{70}Fe_{30}$ electrode (9 ± 2 mV).

Within this narrower potential window in comparison to Fig. 1, the overall activation is expectedly lower. As we have shown previously by quantifying Fe dissolution through coupling the electrochemical measurements with ICP-OES, the reduced lower potential limit especially benefits the dissolution of Fe in the $Ni_{70}Fe_{30}$ bulk electrode, leading to a roughening of the surface and improving the Ni-to-Fe ratio for OER activity [14]. It was also shown that non-Fe-containing electrodes are less sensitive to the lower potential limit, which could explain the higher activation for the coated catalyst studied here. On the other hand, as $NiCoO_2$ already is in an oxidized state, restructuring of the anhydrous oxide to a hydrous oxide might be a slower process than on the metal-electrode. Thus, to further increase the conditioning effect, we extended the conditioning from 46 to 300 cycles. With such a prolonged conditioning time of 2.8 h, a significantly higher activation of 27 ± 4 mV at 10 mA cm^{-2} for $NiCoO_2$ could be achieved.

Next, the impact of the lower potential limit as well as the scan rate was studied for the powder-based electrodes and compared to the conventional conditioning (with only 46 cycles) of $Ni_{70}Fe_{30}$ (Fig. 3 and Figure S8). While a direct comparison of the absolute activation is difficult due to the different conditioning times and surface structures, activation trends can well be compared. The large potential window from −0.35 – 1.6 V was tested both at 10 mV s^{-1} (SEQ01) as well as 100 mV s^{-1} (SEQ02). The previously employed mild conditioning, now with 300 cycles, is termed SEQ03. As the number of cycles is held constant, the different conditioning parameters led to different conditioning times of 32.5 h, 3.25 h and 18.3 h for SEQ01, SEQ02 and SEQ03, respectively.

It can be observed that, even though $NiCoO_2$ does not contain Fe, the trend that a low lower potential limit (SEQ01 and SEQ02) is favorable for catalyst activation seems to be also valid for the powder-based material. From SEQ03 to SEQ01 the activation is almost doubled to a maximum of 51 ± 5 mV.

Interestingly, a higher activation is present for the powder-based anodes when conditioning with SEQ01 compared to conditioning with SEQ02, while this is not the case for the $Ni_{70}Fe_{30}$ electrode. It might be argued that the slower scan rate is beneficial for the re-arrangement of the anhydrous oxide. However, it needs to be noted that the coatings delaminated for SEQ01 and SEQ02, probably due to the strong gas evolution during the conditioning into the HER. This can be observed optically by the light area of the Ni-support after conditioning (Figure S9). As a result, we assume that the measured activation does not solely reflect the behavior of the powder itself but that of the combined system, consisting of the catalyst layer and the Ni99.2 support material. A comparison with the conditioning data of a Ni99.99 electrode from Gohlke et al. [14], further supports the hypothesis that activation is predominantly influenced by the support, since the same strong dependency on the scan rate for the Ni99.99 electrode was observed. Thus, to study the real activation behavior of powder-based catalyst layers, the delamination issue needs to be addressed. The delamination itself might be attributed to the additional formation of hydrogen bubbles, which adhere to the surface, introducing significant mechanical stress within the porous structure and leading to subsequent potential detachment of catalyst particles. The dynamics of bubble formation, growth, and detachment are influenced by factors such as wettability and surface structure of the materials [12,37,38]. Hydrogen bubbles, in particular, might cause substantial mechanical stress compared to oxygen bubble formation, because of their rapid nucleation and smaller detachment size [39]. While particle detachment is also visible for SEQ03, which cycles only into the OER regime, the extent of delamination is less. Oxygen bubbles may have a different impact due to changed nucleation, growth and surface property characteristics combined with a reduced total bubble load. Therefore, our results strongly underpin that understanding and controlling bubble dynamics is crucial for improving the stability and performance of powder-based anodes. In a follow-up study, we plan to employ Laser Marked Shadowgraphy and Glare Point Velocimetry, to better visualize the bubble growth and detachment from the electrode.

3.3. Catalyst-layer optimization

To improve the stability and adhesion of the catalyst layer, ball milling (BM) of the catalyst particles before ink preparation and coating as well as plasma treatment (PT) of the catalyst layers after coating are investigated. Fig. 4 presents the stability of the differently prepared layers during a 2 h CP conducted at 100 mA cm^{-2} from the last cycle of the PAD protocol (see SI, section S3). These are compared to the pure

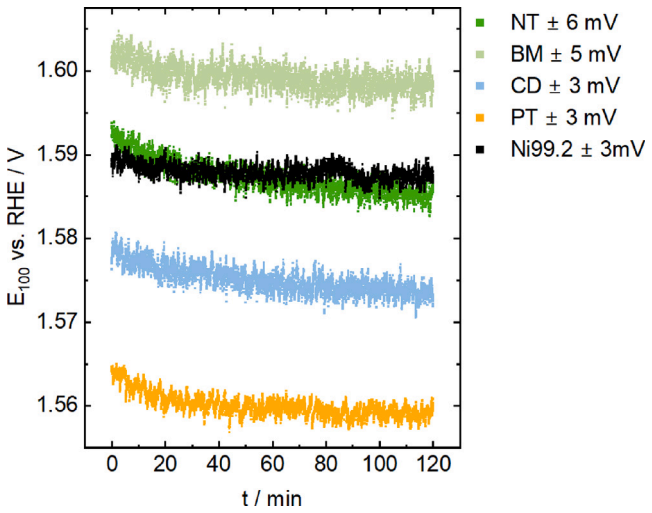

Fig. 4. Comparison of 2 h CPs at 100 mA cm^{-2} for $NiCoO_2$ catalyst layers with different pre-treatment methods: no treatment (NT), ball milling (BM), electrochemically conditioning (CD), plasma treatment (PT). The 2 h CP of Ni99.2 is added as point of reference. The shown CP is the final of four CPs, as defined for the PAD protocol (see SI, section S3). The CD sample was conditioned with SEQ03 (0.5 – 1.6 V vs. RHE, 10 mV s^{-1}, 300 cycles). The given standard deviation is the mean value of the standard deviation in every time step.

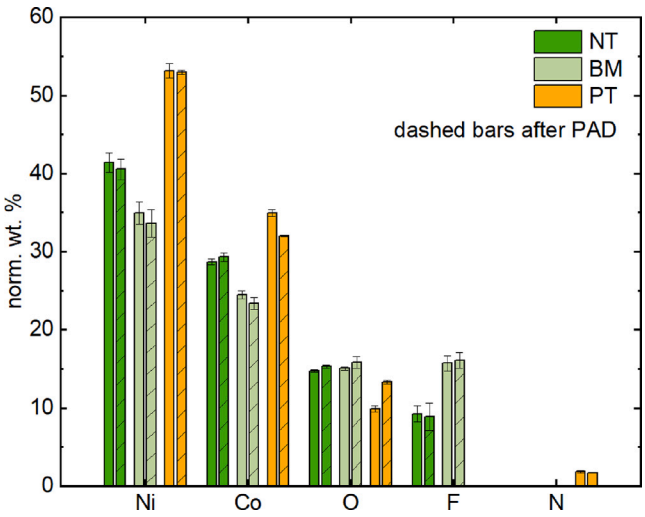

Fig. 5. EDX analysis of elemental composition of NT, BM, and PT samples before and after activity determination protocol. Please note that Zr, S and C are not shown here for better visibility. The full data set can be found in Figure S10.

Ni99.2 support, the unconditioned, regularly prepared catalyst layer (no treatment, NT) as well as the sample conditioned by SEQ03 (CD).

All electrodes investigated demonstrate stable performance over the examined timeframe with most of them even exhibiting slight activation behavior, except for Ni99.2, which maintains a constant potential. However, a clear difference in performance is observed among the different pre-treatment techniques, with the PT electrode showing the highest activity, i.e., the lowest potential of 1.56 V, followed by the CD electrode. The NT electrode and Ni99.2 exhibit similar performances, while the BM electrode shows the lowest activity with 1.60 V.

The relatively good performance of Ni99.2 can be attributed to its inherent activity as a support material, particularly in the presence of Fe in the electrolyte (200 ppb) [40,41]. Additionally, the brief initial conditioning step in the electrochemical protocol (see SI, section S3) may already facilitate the formation of active species, which might explain why Ni99.2 achieves a performance comparable to the NT electrode. Furthermore, the presence of Nafion as a binder in the coated electrodes might reduce the active surface area of the powder catalyst and, thus, its catalytic activity. The presence of the binder is also visible by the clear fluorine signal in the EDX analysis (Fig. 5). Additionally, microstructure plays a critical role in anode performance [12]. Here, the microstructure of the NT electrodes may be unfavorable for gas bubble transport, potentially decreasing the electrodes' activity.

Ball milling leads to a particle size reduction and homogenization of the particle size [25]. Thus, a more homogeneous layer with potentially better adhesion was expected. Contrary to these expectations, partial delamination of the catalyst layer occurred already during the PAD protocol, as shown in Figure S9. Furthermore, it is counterintuitive that, even though much of the layer remains intact, its performance is still lower than that of the support (Ni99.2) itself. According to the EDX analysis (Fig. 5), this could be explained by a comparable high binder content in the resulting layers, blocking the availability of active sites in the liquid alkaline environment.

Compared to the NT electrodes (9 wt.% F), a significantly higher binder content (16 wt.% F) is present in the BM electrodes. The reason for this remains unclear given that the absolute binder content in the catalyst ink was kept constant. Variations in coating morphology or the interfacial interaction between binder and particle surface might have led to more Nafion being exposed for the EDX measurement. Additionally, inconsistencies in the catalyst ink preparation or cross contaminations during the ball milling process cannot be excluded. The EDX analysis, furthermore, revealed the presence of zirconium (Zr) impurities in the BM electrodes (see Figure S10a for full EDX data), which likely originates from the ball milling process owing to abrasion from the zirconium-based milling balls. However, this contamination is not expected to negatively impact the OER performance [42].

As demonstrated in our previous work, the enhanced performance of the CD electrodes likely arises from the formation of a hydrous oxide layer during conditioning. This was confirmed by XPS, which revealed an increase in hydroxide species on bulk electrodes after conditioning [14]. Given the similar nickel-rich surface structure of our spray-coated $NiCoO_2$ anodes, we expect a similar activation mechanism to occur. Furthermore, a recent study on different Ni-based thin-film electrodes report formation of oxyhydroxide species under electrochemical conditioning, independent from the initial material composition [43]. Accordingly, we expect that the coated electrodes exhibit not only Ni–OOH but also a complementary Co–OOH contribution.

The PT electrodes show the best performance, even surpassing the CD electrodes, which is attributed to several factors. First, enhanced (nano-)porosity stemming from the plasma treatment (as seen in Figure S15) is likely to increase the active surface area [27,33]. Additionally, the removal of the binder – evidenced by the absence of fluorine (F) in the EDX analysis – increases the accessibility of active sites for the OER. Plasma treatment also reduces the initial oxygen content, likely due to the formation and subsequent removal of gaseous NO species during the treatment. Moreover, nitrogen from the plasma is incorporated into the structure, which is even sustained after the PAD protocol (Fig. 5, dashed bar). As previously discussed, nitrogen doping may positively influence the performance by creating oxygen vacancies [33,44]. After the PAD protocol, the PT electrode revealed the most significant increase in O content compared to NT, BM and CD electrodes. This supports the hypothesis of a facilitated formation of active (an)hydrous oxide layers possibly because of nitrogen incorporation. However, a distinct observation is that the PT sample also shows the largest decrease in Co content post-measurement, suggesting that cobalt is either leached out or redistributed. Our previous in-depth analysis of the effect of plasma treatment on our coated layers [27] further revealed that while plasma treatment does not alter the bulk crystal

structure (confirmed by X-ray diffraction), it creates a more structurally "flexible" electrode that undergoes reversible phase transformations during electrochemical cycling, facilitating the formation of active NiOOH/CoOOH species (as seen during *operando* Raman spectroscopy). Finally, we also showed that plasma treatment leads to a complete change in the wetting behavior of the anode, which could improve gas bubble detachment and, hence, increase the activity [12,27].

The analysis of the electrodes' morphology is depicted in Figure S11 (a, b) (CD electrode), and Figure S12 (NT, PT and BM electrodes). The SEM images reveal that the NT electrode exhibits an ordered porous structure with concave, hemispherical pores. This microstructure remains intact after plasma treatment; however, as we showed previously, increased pore formation is visible at the nanoscale [27]. This increased porosity likely increases the active surface area, which is in line with the increased performance for the PT electrodes.

In contrast, BM electrodes lack a structured surface and appear to have larger agglomerates formed during the drying process of the coating. Conversely, we observe smaller particle sizes for the ball milled powder prior to coating, which becomes apparent from the longer sedimentation time in the transmittograms (Figure S13) [45,46]. The decreased particle size may give a larger surface area for possible interaction with Nafion. This supports our assumption that the resulting coating microstructure might play a role in the detection of an increased binder content.

After the PAD protocol, the structures of the coatings stay intact for NT and PT electrodes as well as for the remaining catalyst layers of the CD-SEQ03 and BM electrodes (Figure S11(b) and S12(d, e, f)). The unchanged microstructure is in line with the constant measured potential during the CP measurements (Fig. 4), since a change of microstructure would be expected to show a deactivation of the materials and a subsequent potential increase. The mechanical stability of PT electrodes was investigated by a cavitation erosion test. Here, the electrodes are exposed to cavitation bubbles generated by an ultrasonic horn, which simulates accelerated electrode aging under increased gas formation. We showed that PT electrodes exhibit stronger resistance to layer detachment compared to their NT counterparts. As we discussed in a previous work, the enhanced contact between the coating and the support arises from the energy input from the plasma, upon which a sintering of the coating occurs [27]. This leads to an improved cohesion of the coating particles, and thus an overall increase in mechanical stability. Additionally, since both coating and substrate contain Nickel, a layer rearrangement occurs, which enhances the contact between surface and coating by a sintering process, thereby increasing the adhesion. For more information see section S13, Figure S14 and Figure S15.

3.4. Combining plasma treatment and electrochemical conditioning

Since both plasma treatment and electrochemical conditioning have independently demonstrated promising results with respect to the pre-activation of powder-based electrodes, their combination to further optimize the catalyst's pre-treatment was investigated. Also, the mechanical stabilization of the catalyst layers by plasma treatment makes these electrodes potentially interesting for pairing with a more intensive conditioning protocol. For that purpose, we chose two conditioning protocols in combination with the plasma treatment: SEQ01, which generally yields the best activation but leads to delamination on the NT electrodes, and SEQ03, which offers stable layers but typically leads to less activation. Fig. 6 displays the activation of $NiCoO_2$ exclusively conditioned electrochemically with SEQ01 and SEQ03 (CD $NiCoO_2$), as well as the additionally plasma-treated sample (PT-CD $NiCoO_2$). Moreover, their performance is evaluated against the conditioned support material (CD Ni99.2). The respective conditioning CVs are given in Figure S16.

Unfortunately, the improved adhesion strength of the PT electrodes did not fully prevent the delamination of the catalyst layer during

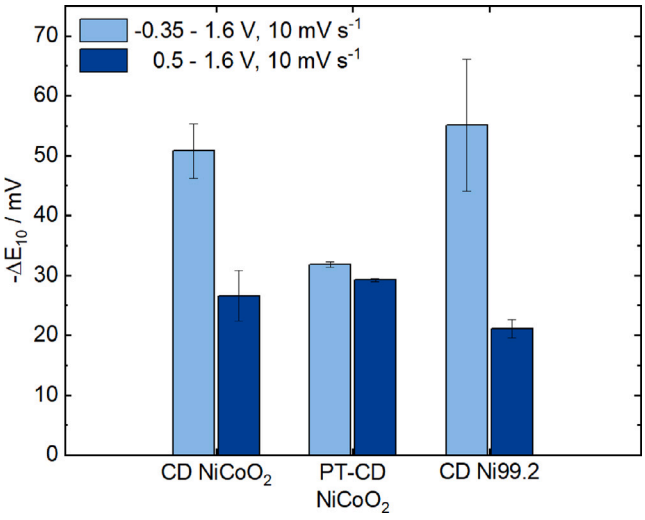

Fig. 6. Activation ($-\Delta E_{10}$) at 10 mA cm^{-2} of conditioned $NiCoO_2$, additionally plasma-treated $NiCoO_2$ and conditioned Ni99.2. SEQ01 (−0.35 – 1.6 V vs. RHE, 10 mV s^{-1}) and SEQ03 (0.5 – 1.6 V vs. RHE, 10 mV s^{-1}) and 300 cycles were used for conditioning.

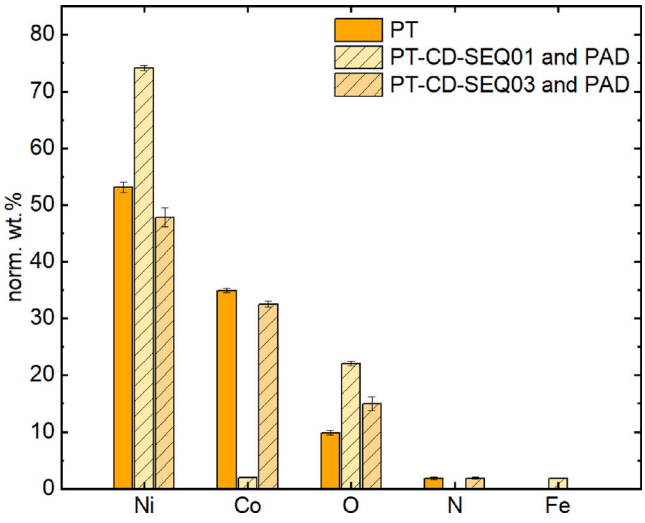

Fig. 7. EDX determination of elemental composition of PT samples before the PAD protocol and after further conditioning with SEQ01 and SEQ03 after the PAD protocol.

conditioning with SEQ01, however, minor amounts of catalyst particles remain (Figure S9 and S11(c)). In contrast, the PT electrode conditioned with SEQ03 remained intact, confirming our expectations of enhanced catalyst layer stability. Still, a slightly larger activation is observed for conditioning with SEQ01. Yet, due to the catalyst delamination, it remains unclear whether the measured activation reflects the catalyst layer itself or the underlying support. The activation trend for the PT-CD electrodes is analogous to the CD electrodes, but the difference between SEQ01 and SEQ03 becomes less pronounced for the PT-CD electrodes. Specifically, the activation after conditioning the PT electrodes with SEQ01 is significantly lower compared to their CD counterparts, while the activation by CD-SEQ03 remains largely unchanged upon pre-treatment with plasma. This suggests that, despite delamination cannot be fully prevented, it is less severe for PT electrodes, allowing for at least partial activation of the powder layer. It is, furthermore, worth comparing the extent of activation of CD-SEQ01 and PT-CD-SEQ01 to the pure CD Ni99.2 support. CD-SEQ01

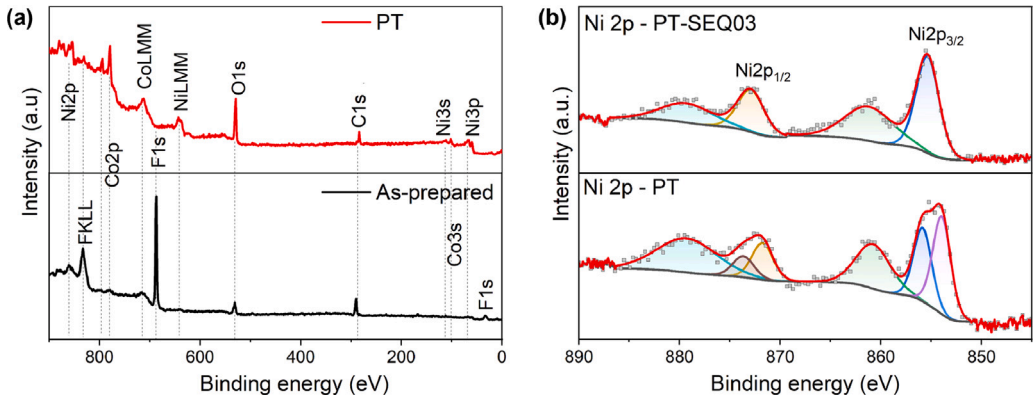

Fig. 8. (a) XPS survey spectra of PT and NT samples with significant elemental peaks marked and (b) high-resolution XPS showing the Ni 2p region of the PT and PT-SEQ03 electrodes.

$NiCoO_2$ and CD-SEQ01 Ni99.2 show similar activation, while that of PT-CD-SEQ01 $NiCoO_2$ is lower. Considering a possible fast delamination of CD-SEQ01 $NiCoO_2$, the extent of activation could be fully assigned to the conditioning of the Ni99.2 support, explaining their similar extents. On the other hand, for PT-CD-SEQ01 $NiCoO_2$, initial particle adhesion might have been improved, potentially allowing some powder activation during conditioning. Nevertheless, this activation is followed by a gradual detachment, which leads to exposure of the Ni99.2 support. The remaining cycles then activate the support, but to a lesser extent than what a full CD-SEQ01 Ni99.2 electrode experiences. Fig. 7 depicts the EDX analysis of the PT and PT-CD electrodes. It supports the assumption that plasma treatment enhances the catalyst layer adhesion, as small amounts of cobalt remain detectable even after CD-SEQ01. Furthermore, the layers remain entirely intact after CD-SEQ03. Additionally, a slight presence of Fe is detected after CD-SEQ01, which is consistent with the findings of Vinayakumar et al. [27] The increased porosity of the samples after plasma treatment likely enhances Fe uptake in the low potential region, which, in turn, directly improves OER activity. This underscores the importance of optimizing conditioning parameters for forming highly active OER sites [43].

To elucidate the surface oxidation state after the combined plasma treatment and electrochemical conditioning, XPS characterization was performed on freshly coated (as-prepared), PT and PT-CD-SEQ03 electrodes. Fig. 8 summarizes the XPS results. The survey spectra (Fig. 8(a)) show pronounced changes in surface chemistry after plasma treatment. Consistent with earlier findings [27], the treatment removes the Nafion binder from the electrode surface demonstrated by the complete loss of the characteristic F 1s signal at ~690 eV that was clearly present in the as-prepared sample. This observation supports the EDX results shown in Fig. 5.

The high-resolution Ni 2p spectra (Fig. 8(b)) provide insights into the chemical state evolution of nickel species throughout the plasma treatment and electrochemical conditioning. The PT sample exhibits deconvoluted Ni $2p_{3/2}$ and Ni $2p_{1/2}$ peaks at ~855 eV and ~873 eV characteristic of a Ni^{2+} species (NiO) and one higher oxidized species such as $Ni(OH)_2$ or NiOOH.[14,27]. Notably, after additional conditioning with SEQ03, the Ni 2p spectrum shows a redistribution of peak intensities with an enhanced contribution from higher binding energy components. This shift suggests partial oxidation of the Ni species during the conditioning, consistent with the formation of catalytically active NiOOH phases that are known to be central to the OER mechanism. Because of the similar binding energies of Co^{2+} and Co^{3+}, the deconvoluted Co 2p spectrum (Figure S17) cannot be reliably used to assign the cobalt oxidation state in $NiCoO_2$[47,48]. Nevertheless, a general surface reconstruction away from the initial metal oxide state is indicated by changes in the satellite features of the Co 2p spectrum. Before electrochemical conditioning, the electrodes exhibit pronounced satellite peaks at ~783 eV (for Co $2p_{3/2}$) and ~803 eV (for Co $2p_{1/2}$), which disappear after conditioning, consistent with a less complex coordination environment than typically observed for metal oxides [49,50].

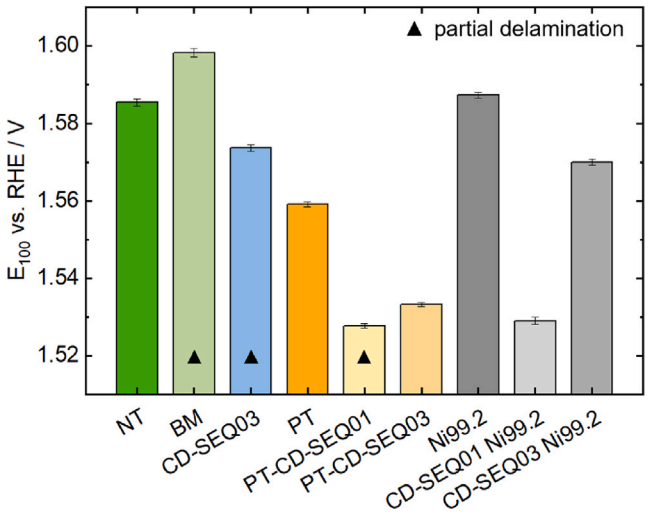

Fig. 9. Mean potential of the final 20 min of a 2 h CP at 100 mA cm^{-2} for tested $NiCoO_2$ electrodes. The chosen CP is the final of four CPs, as defined in the PAD protocol (see SI, section S3). Conditioning performed with SEQ01 (−0.35 – 1.6 V vs. RHE, 10 mV s^{-1}) and SEQ03 (0.5 – 1.6 V vs. RHE, 10 mV s^{-1}) in 1 M KOH at RT with 300 cycles. The delamination of the respective electrodes is indicated in the legend. Marks are signifying the observation of delamination.

Finally, the O 1s XPS spectra of the PT samples, shown in Figure S18(b) exhibit deconvoluted components at ~529.2 eV and ~531 eV, attributed to lattice oxygen (O^{2-}) and surface hydroxyl groups (OH^-), respectively, indicative of a hydroxylated mixed-metal oxide surface [50]. Following the electrochemical conditioning (Figure S18(a), PT-SEQ03), these features persist with notable intensity redistribution towards higher availability of hydroxyl species, while an additional signal emerges at ~532.1 eV, assigned to weakly adsorbed oxygen species including physisorbed water adsorbates. This spectral evolution is widely interpreted as evidence of dynamic surface reconstruction and the formation of oxyhydroxide phases, such as NiOOH or CoOOH [51–53]. The XPS investigations align well with our previous work [14], confirming our assumptions for the improved OER performance of CD electrodes.

To ultimately draw conclusions about the efficiency of the different pre-treatment methods, the absolute potentials of the PAD protocol were compared. Fig. 9 presents the potential at 100 mA cm^{-2} (E_{100}) after

Table 1
OER overpotential at 10 mA cm^{-2} and 100 mA cm^{-2} derived from activity determination by CV measurements.

Sample	η_{10}/mV	η_{100}/mV
PT-CD-SEQ01 $NiCoO_2$	250 ± 6	294 ± 9
PT-CD-SEQ03 $NiCoO_2$	264 ± 3	308 ± 2
CD-SEQ01 Ni99.2	247 ± 6	292 ± 5
CD-SEQ03 Ni99.2	289 ± 1	343 ± 1

the final 2 h CP measurement for all analyzed electrodes. It becomes again evident that all CD electrodes show improved activity, i.e., lower potentials, regardless of any layer detachments. As previously noted, the BM electrodes exhibit the lowest activity among all measured electrodes. Notably, the CD-SEQ01 Ni99.2 support demonstrates potentials comparable to the PT-CD-SEQ01 electrode probably due to the delamination of the catalyst layer.

However, when comparing the potential of the PT-CD-SEQ03 electrodes, where the catalyst layer stayed intact, to that of the CD-SEQ03 Ni99.2 support, the powder-coated anode shows a significantly better performance, i.e., a potential difference of 37 mV. These findings suggest that conditioning the powder-coated anodes with SEQ01 – while preventing layer delamination – could potentially lead to an even higher activity gain. The OER performance of the PT-CD electrodes, presented as overpotential (η) at 10 and 100 mA cm^{-2}, is compared to the conditioned Ni99.2 in Table 1. The results clearly indicate that the combination of plasma treatment and electrochemical conditioning yields notable OER performance, comparable to recent reports on Fe-free Ni–Co oxides (η_{10} = 320 mV) [54], and competitive with state-of-the-art Ni–Fe-LDH electrodes (η_{10} = 243 mV) [55].

Our results demonstrate that the combined effect of electrochemical conditioning and plasma treatment can lead to significant activity increases. Moreover, as we demonstrated in our previous works, optimizing coating conditions to enhance microstructural properties can elevate the performance even more [12,27]. This effect, driven by the fabrication process and supported by stable catalyst layers, can still be exploited for future works. This highlights the importance of careful catalyst preparation along the entire production chain, especially putting a focus on obtaining stable anode layers.

4. Conclusion

In this work, electrochemical conditioning, originally optimized for bulk electrodes, was translated to Ni- and Co-based powder-coated anodes, clearly improving their electrochemical activity for the OER. Longer treatment times are necessary to effectively activate those electrodes as, compared to bulk metal electrodes, they are already in an anhydrous oxide state and reconstruction into the active hydrous phase requires more intense treatment. According to our previous insights, larger potential windows should enhance the restructuring process. However, adhesion of the catalyst layer was challenging when cycling into the HER regime. This delamination is likely caused by the high mechanical stress exerted on the porous anode layers during gas evolution. To enhance the adhesion, we investigated additional pre-treatment methods such as ball milling of the catalyst powder before coating as well as plasma treatment of the coated catalyst layers. While ball milling proved useful for reducing initial particle size, the resulting electrodes showed a decreased performance, which is supposedly related to a stronger coverage of the particles by the added binder. Also, delamination was still observed.

Plasma treatment successfully improved both the activity as well as the mechanical stability. This method has previously been shown to enhance the active surface area by introducing nanoscale porosity as well as removing excess binder from the catalyst layers [27,33]. This resulted in a higher relative content of active Ni and Co species. The incorporation of nitrogen presumably further contributed to improved performance by promoting the formation of oxygen vacancies. This enhancement is also observed for the catalyst layers studied, additionally reducing delamination by an improved mechanical adhesion of the catalyst layer to the support.

Finally, plasma pre-treated electrodes were subjected to electrochemical conditioning combining the positive effects of both techniques. While an improved stability of the catalyst layers was observed, the delamination within the extended potential window could not fully be prevented. Thus, besides the activation of the catalyst, the activation procedure also significantly affects the support leading to similar final activities with and without the catalyst layer. However, with the mild conditioning protocol, the catalyst-coated electrode clearly surpassed the similarly conditioned Ni99.2 support. In comparison to the untreated powder-coated electrode, an activity improvement of more than 30 mV at 100 mA cm^{-2} could be achieved by plasma treatment in combination with mild conditioning. This holds the promise that more intense conditioning on stabilized electrodes could even further boost the performance. The XPS analysis supports these conclusions by revealing that plasma-treated and subsequently conditioned electrodes undergo additional surface reconstruction during operation. This is visible in the enhanced O 1s signal and the shift in Ni oxidation states, which indicate the in-situ formation of catalytically active oxyhydroxide species.

Overall, our findings suggest that the formation of the active catalyst layer is strongly influenced by pre-treatment conditions. Careful optimization of treatment protocols can significantly enhance activity, as well as chemical and mechanical stability. Future works should focus on stabilizing catalyst layers and investigating the underlying mechanisms governing catalyst layer delamination to fully exploit the promising combined effects of plasma treatment and electrochemical conditioning.

CRediT authorship contribution statement

Christian Marcks: Writing – review & editing, Writing – original draft, Visualization, Validation, Methodology, Investigation, Formal analysis, Data curation, Conceptualization. **Clara Gohlke:** Writing – review & editing, Validation, Methodology, Formal analysis, Conceptualization. **Mohit Chatwani:** Writing – review & editing, Visualization, Validation, Methodology, Formal analysis, Data curation. **Adarsh Jain:** Writing – review & editing, Methodology. **Timo Wagner:** Writing – review & editing, Methodology, Formal analysis. **Nicolas Wöhrl:** Writing – review & editing, Supervision, Software, Resources, Project administration, Methodology, Funding acquisition, Formal analysis. **Vineetha Vinayakumar:** Writing – review & editing, Visualization, Validation, Supervision, Project administration, Methodology, Formal analysis, Data curation. **Vera Seidl:** Writing – review & editing, Visualization, Supervision, Investigation, Formal analysis, Data curation, Project administration. **Doris Segets:** Writing – review & editing, Validation, Supervision, Software, Resources, Project administration, Methodology, Funding acquisition. **Anna K. Mechler:** Writing – review & editing, Validation, Supervision, Software, Resources, Project administration, Methodology, Investigation, Funding acquisition, Formal analysis, Conceptualization.

Declaration of Generative AI and AI-assisted technologies in the writing process

During the preparation of this work the authors used ChatGPT in order to spell check, as well as improve the language of the manuscript. After using this tool, the authors reviewed and edited the content as needed and take full responsibility for the content of the publication.

Declaration of competing interest

The authors declare that they have no known competing financial interests or personal relationships that could have appeared to influence the work reported in this paper.

Acknowledgments

We acknowledge financial support from the German Federal Ministry of Research, Technology and Space (BMFTR project "PrometH2eus", FKZ 03HY105A, 03HY105F). We gratefully acknowledge the support of Blaz Toplak for analyzing XPS data and the support from Raphael Diebold with performing electrochemical measurements. Open Access funding enabled and organized by Projekt DEAL.

Appendix A. Supplementary data

Supplementary material related to this article can be found online at https://doi.org/10.1016/j.ijhydene.2026.154578.

Data availability

The data that support the findings of this study is openly available in Zenodo [56].

References

[1] Li X, Walsh FC, Pletcher D. Nickel based electrocatalysts for oxygen evolution in high current density, alkaline water electrolysers. Phys Chem Chem Phys 2011;13(3):1162–7. http://dx.doi.org/10.1039/c0cp00993h.
[2] Long X, Li J, Xiao S, Yan K, Wang Z, Chen H, Yang S. A strongly coupled graphene and FeNi double hydroxide hybrid as an excellent electrocatalyst for the oxygen evolution reaction. Angew Chem Int Ed 2014;53(29):7584–8. http://dx.doi.org/10.1002/anie.201402822.
[3] Wu G, Li N, Zhou D-R, Kurachi M, Xu B-Q. Anodically electrodeposited Co+Ni mixed oxide electrode: preparation and electrocatalytic activity for oxygen evolution in alkaline media. J Solid State Chem 2004;177(10):3682–92. http://dx.doi.org/10.1016/j.jssc.2004.06.027.
[4] Burke MS, Enman LJ, Batchellor AS, Zou S, Boettcher SW. Oxygen evolution reaction electrocatalysis on transition metal oxides and (Oxy)hydroxides: Activity trends and design principles. Chem Mater 2015;27(22):7549–58. http://dx.doi.org/10.1021/acs.chemmater.5b03148.
[5] Thenuwara AC, Attanayake NH, Yu J, Perdew JP, Elzinga EJ, Yan Q, Strongin DR. Cobalt intercalated layered NiFe double hydroxides for the oxygen evolution reaction. J Phys Chem B 2018;122(2):847–54. http://dx.doi.org/10.1021/acs.jpcb.7b06935.
[6] Dionigi F, Zeng Z, Sinev I, Merzdorf T, Deshpande S, Lopez MB, Kunze S, Zegkinoglou I, Sarodnik H, Fan D, Bergmann A, Drnec J, de Araujo JF, Gliech M, Teschner D, Zhu J, Li W-X, Greeley J, Cuenya B Roldan, Strasser P. In-situ structure and catalytic mechanism of NiFe and CoFe layered double hydroxides during oxygen evolution. Nat Commun 2020;11(1):2522. http://dx.doi.org/10.1038/s41467-020-16237-1.
[7] Bates MK, Jia Q, Doan H, Liang W, Mukerjee S. Charge-transfer effects in Ni–Fe and Ni–Fe–Co mixed-metal oxides for the alkaline oxygen evolution reaction. ACS Catal 2016;6(1):155–61. http://dx.doi.org/10.1021/acscatal.5b01481.
[8] Lindstrom ML, Gakhar R, Raja K, Chidambaram D. Facile synthesis of an efficient Ni–Fe–Co based oxygen evolution reaction electrocatalyst. J Electrochem Soc 2020;167(4):046507. http://dx.doi.org/10.1149/1945-7111/ab6b08.
[9] Feng C, Wang F, Liu Z, Nakabayashi M, Xiao Y, Zeng Q, Fu J, Wu Q, Cui C, Han Y, Shibata N, Domen K, Sharp ID, Li Y. A self-healing catalyst for electrocatalytic and photoelectrochemical oxygen evolution in highly alkaline conditions. Nat Commun 2021;12(1):5980. http://dx.doi.org/10.1038/s41467-021-26281-0.
[10] de Groot MT. Alkaline water electrolysis: with or without iron in the electrolyte?. Curr Opin Chem Eng 2023;42:100981. http://dx.doi.org/10.1016/j.coche.2023.100981.
[11] Electrode Package - The heart of Electrolyzer. No. ETR-EP2405002. https://energytransition.denora.com/en/offerings/electrode-package (zugegriffen am 06.03.2025).
[12] Jain A, Marcks C, Grebener L, Johny J, Odungat AS, Chatwani M, Kräenbring M-A, Shaji A, Tesch MF, Mechler AK, Vinayakumar V, Segets D. A proof–of–principle demonstration: Exploring the effect of anode layer microstructure on the alkaline oxygen evolution reaction. Adv Funct Mater 2025. http://dx.doi.org/10.1002/adfm.202421352.
[13] Deo Y, Thissen N, Seidl V, Gallenberger J, Hoffmann J, Hofmann JP, Etzold BJM, Mechler AK. Thin nickel coatings on stainless steel for enhanced oxygen evolution and reduced iron leaching in alkaline water electrolysis. Electrochem Sci Adv 2024. http://dx.doi.org/10.1002/elsa.202400023.
[14] Gohlke C, Gallenberger J, Niederprüm N, Ingendae H, Kautz J, Hofmann JP, Mechler AK. Boosting the oxygen evolution reaction performance of Ni–Fe–Electrodes by tailored conditioning. ChemElectroChem 2024. http://dx.doi.org/10.1002/celc.202400318.
[15] Thongmee S, Pang HL, Yi JB, Ding J, Lin JY, Van LH. Unique nanostructures in NiCo alloy nanowires. Acta Mater 2009;57(8):2482–7. http://dx.doi.org/10.1016/j.actamat.2009.02.006.
[16] Cheng M, Wen M, Zhou S, Wu Q, Sun B. Solvothermal synthesis of NiCo alloy icosahedral nanocrystals. Inorg Chem 2012;51(3):1495–500. http://dx.doi.org/10.1021/ic201763j.
[17] Zhang Y-C, Han C, Gao J, Pan L, Wu J, Zhu X-D, Zou J-J. NiCo-based electrocatalysts for the alkaline oxygen evolution reaction: A review. ACS Catal 2021;11(20):12485–509. http://dx.doi.org/10.1021/acscatal.1c03260.
[18] Babar N-U-A, Joya KS. Spray-coated thin-film Ni-oxide nanoflakes as single electrocatalysts for oxygen evolution and hydrogen generation from water splitting. ACS Omega 2020;5(19):10641–50. http://dx.doi.org/10.1021/acsomega.9b02960.
[19] Qu Y, Gomaa MM, Sayed MH, Boshta M, Greczynski G, Yakimova R, Sun J. A comparative study of NiCo 2 O 4, NiO, and Co 3 O 4 electrocatalysts synthesized by a facile spray pyrolysis for electrochemical water oxidation. Adv Mater Interfaces 11(8):2024. http://dx.doi.org/10.1002/admi.202300920.
[20] Fu Y, Yu H-Y, Jiang C, Zhang T-H, Zhan R, Li X, Li J-F, Tian J-H, Yang R. NiCo alloy nanoparticles decorated on N–doped carbon nanofibers as highly active and durable oxygen electrocatalyst. Adv Funct Mater 28(9):2018. http://dx.doi.org/10.1002/adfm.201705094.
[21] Singh SK, Kumar D, Dhavale VM, Pal S, Kurungot S. Strategic preparation of efficient and durable NiCo alloy supported N–doped porous graphene as an oxygen evolution electrocatalyst: A theoretical and experimental investigation. Adv Mater Interfaces 3(20):2016. http://dx.doi.org/10.1002/admi.201600532.
[22] Liu Z, Tan H, Liu D, Liu X, Xin J, Xie J, Zhao M, Song L, Dai L, Liu H. Promotion of overall water splitting activity over a wide pH range by interfacial electrical effects of metallic NiCo-nitrides nanoparticle/NiCo2O4 nanoflake/graphite fibers. Adv Sci 2019;6(5):1801829. http://dx.doi.org/10.1002/advs.201801829.
[23] Chen Z, Cai L, Yang X, Kronawitter C, Guo L, Shen S, Koel BE. Reversible structural evolution of NiCoO x H y during the oxygen evolution reaction and identification of the catalytically active phase. ACS Catal 2018;8(2):1238–47. http://dx.doi.org/10.1021/acscatal.7b03191.
[24] Jiang T, Ansar S-A, Yan X, Chen C, Fan X, Razmjooei F, Reisser R, Montavon G, Liao H. In situ electrochemical activation of a codoped heterogeneous system as a highly efficient catalyst for the oxygen evolution reaction in alkaline water electrolysis. ACS Appl Energy Mater 2019;2(12):8809–17. http://dx.doi.org/10.1021/acsaem.9b01807.
[25] Bhandari S, Schierholz R, Eichel R-A, Luna AL, Mechler AK. Exploring the effect of ball milling on the physicochemical properties and oxygen evolution reaction activity of nickel and cobalt oxides. Adv Energy Sustain Res 5(12):2024. http://dx.doi.org/10.1002/aesr.202400183.
[26] Xu L, Jiang Q, Xiao Z, Li X, Huo J, Wang S, Dai L. Plasma-engraved Co3 O4 nanosheets with oxygen vacancies and High Surface Area for the oxygen evolution reaction. Angew Chem Int Ed 2016;55(17):5277–81. http://dx.doi.org/10.1002/anie.201600687.
[27] Vinayakumar V, Wagner T, Marcks C, Johny J, Wartner G, Lim A, Tesch MF, Spanos I, Ghafari A, Jain A, Prymak O, Sanjuán I, Odungat AS, Anwar O, Chatwani M, Jose A, Chanda V, Knop-Gericke A, Andronescu C, Mechler AK, Wöhrl N, Segets D. Ni-Co-O anodes for the alkaline oxygen evolution reaction: Multistage electrode optimization and plasma-assisted activity enhancement enabled by a coherent workflow. Chem Eng J 167169:2025. http://dx.doi.org/10.1016/j.cej.2025.167169.
[28] Chattot R, Roiron C, Kumar K, Martin V, Campos Roldan CA, Mirolo M, Martens I, Castanheira L, Viola A, Bacabe R, Cavaliere S, Blanchard P-Y, Dubau L, Maillard F, Drnec J. Break-in bad: On the conditioning of fuel cell nanoalloy catalysts. ACS Catal 2022;12(24):15675–85. http://dx.doi.org/10.1021/acscatal.2c04495.
[29] Fugane K, Mori T, Ou DR, Yan P, Ye F, Yoshikawa H, Drennan J. Improvement of cathode performance on Pt-CeO(x) by optimization of electrochemical pretreatment condition for PEFC application. Langmuir 2012;28(48):16692–700. http://dx.doi.org/10.1021/la302912r.
[30] Jiang H, Yan L, Zhang S, Zhao Y, Yang X, Wang Y, Shen J, Zhao X, Wang L. Electrochemical surface restructuring of phosphorus-doped Carbon@MoP electrocatalysts for hydrogen evolution. Nano-Micro Lett 2021;13(1):215. http://dx.doi.org/10.1007/s40820-021-00737-w.
[31] Oezaslan M, Hasché F, Strasser P. Oxygen electroreduction on Pt x Co 1-x and Pt x Cu 1-x alloy nanoparticles for basic and acidic PEM fuel cell. ECS Trans 2011;41(1):1659–68. http://dx.doi.org/10.1149/1.3635697.
[32] Le HT, Lee JE, Yun SY, Kwon O, Park JK, Jeong YK. Plasma-induced oxygen vacancies in N-doped hollow NiCoPBA nanocages derived from prussian blue analogue for efficient OER in alkaline media. Int J Mol Sci 24(11):2023. http://dx.doi.org/10.3390/ijms24119246.
[33] Wagner T, Schaumburg F, Kensy F, Lorke A, Wöhrl N. Changes: optimizing morphology and chemistry of nickel surfaces by a scalable plasma process for hydrogen electrolyzers. Surf Coat Technol 2025;132056. http://dx.doi.org/10.1016/j.surfcoat.2025.132056.
[34] Thissen N, Hoffmann J, Tigges S, Vogel DAM, Thoede JJ, Khan S, Schmitt N, Heumann S, Etzold BJM, Mechler AK. Industrially relevant conditions in lab–scale analysis for alkaline water electrolysis. ChemElectroChem 11(1):2024. http://dx.doi.org/10.1002/celc.202300432.

[35] Chatwani M, Jain A, Marcks C, Johny J, Grebener L, Yun H, Khan AR, Bendt G, Romeis S, Čolić V, Tesch MF, Mechler AK, Vinayakumar V, Segets D. Mechanochemical activation of nickel oxide: a pivotal step in the process chain enabling binder-free-anodes for alkaline water electrolysis, Preprint, http://dx.doi.org/10.31224/4835.

[36] He Y, Cui Y, Zhao Z, Chen Y, Shang W, Tan P. Strategies for bubble removal in electrochemical systems. Energy Rev 2023;2(1):100015. http://dx.doi.org/10.1016/j.enrev.2023.100015.

[37] Iwata R, Zhang L, Wilke KL, Gong S, He M, Gallant BM, Wang EN. Bubble growth and departure modes on wettable/non-wettable porous foams in alkaline water splitting. Joule 2021;5(4):887–900. http://dx.doi.org/10.1016/j.joule.2021.02.015.

[38] Zhao X, Ren H, Luo L. Gas bubbles in electrochemical gas evolution reactions. Langmuir 2019;35(16):5392–408. http://dx.doi.org/10.1021/acs.langmuir.9b00119.

[39] Liu Y, Li S, Wu H, Shi Y. Experimental investigation and analysis for the bubble size distribution during alkaline water electrolysis by using a wire electrode. DeCarbon 2024;5:100052. http://dx.doi.org/10.1016/j.decarb.2024.100052.

[40] Demnitz M, Lamas YM, Garcia Barros RL, de Leeuw den Bouter A, van der Schaaf J, Theodorus de Groot M. Effect of iron addition to the electrolyte on alkaline water electrolysis performance. iScience 2024;27(1):108695. http://dx.doi.org/10.1016/j.isci.2023.108695.

[41] Anantharaj S, Kundu S, Noda S. The Fe effect : A review unveiling the critical roles of Fe in enhancing OER activity of Ni and Co based catalysts. Nano Energy 2021;80:105514. http://dx.doi.org/10.1016/j.nanoen.2020.105514.

[42] Huang L, Chen D, Luo G, Lu Y-R, Chen C, Zou Y, Dong C-L, Li Y, Wang S. Zirconium-regulation-induced bifunctionality in 3D cobalt-iron oxide nanosheets for overall water splitting. Adv Mater 2019;31(28):e1901439. http://dx.doi.org/10.1002/adma.201901439.

[43] Mattinen M, Schröder J, D'Acunto G, Ritala M, Jaramillo TF, Stevens MB, Bent SF. Dynamics of precatalyst conversion and iron incorporation in nickel-based alkaline oxygen evolution reaction catalysts. Cell Rep Phys Sci 2024;5(11):102284. http://dx.doi.org/10.1016/j.xcrp.2024.102284.

[44] Shalom M, Ressnig D, Yang X, Clavel G, Fellinger TP, Antonietti M. Nickel nitride as an efficient electrocatalyst for water splitting. J Mater Chem A 2015;3(15):8171–7. http://dx.doi.org/10.1039/C5TA00078E.

[45] Maude AD, Whitmore RL. A generalized theory of sedimentation. Br J Appl Phys 1958;9(12):477–82. http://dx.doi.org/10.1088/0508-3443/9/12/304.

[46] Gibbs RJ, Matthews MD. The relationship between sphere size and settling velocity. SEPM J Sediment Res 41:1971. http://dx.doi.org/10.1306/74D721D0-2B21-11D7-8648000102C1865D.

[47] Biesinger MC, Payne BP, Grosvenor AP, Lau LWM, Gerson AR, Smart RStC. Resolving surface chemical states in XPS analysis of first row transition metals, oxides and hydroxides: Cr, Mn, Fe, Co and Ni. Appl Surf Sci 2011;257(7):2717–30. http://dx.doi.org/10.1016/j.apsusc.2010.10.051.

[48] Yang J, Liu H, Martens WN, Frost RL. Synthesis and characterization of cobalt hydroxide, cobalt oxyhydroxide, and cobalt oxide nanodiscs. J Phys Chem C 2010;114(1):111–9. http://dx.doi.org/10.1021/jp908548f.

[49] Subedi A, Yang D, Xu X, Dowben PA. Evidence for phase transitions in CoFe 2 O 4 and NiCo 2 O 4 thin films in temperature-dependent X-ray photoelectron spectroscopy. J Phys D: Appl Phys 2024;57(49):495301. http://dx.doi.org/10.1088/1361-6463/ad5aa8.

[50] Laïk B, Richet M, Emery N, Bach S, Perrière L, Cotrebil Y, Russier V, Guillot I, Dubot P. XPS investigation of Co-Ni oxidized compounds surface using peak-on-satellite ratio, application to Co20Ni80 passive layer structure and composition. ACS Omega 2024;9(39):40707–22. http://dx.doi.org/10.1021/acsomega.4c05082.

[51] Burke MS, Kast MG, Trotochaud L, Smith AM, Boettcher SW. Cobalt-iron (oxy)hydroxide oxygen evolution electrocatalysts: the role of structure and composition on activity, stability, and mechanism. J Am Chem Soc 2015;137(10):3638–48. http://dx.doi.org/10.1021/jacs.5b00281.

[52] Easton CD, Morgan DJ. Critical examination of the use of x-ray photoelectron spectroscopy (XPS) O 1s to characterize oxygen vacancies in catalytic materials and beyond. J Vac Sci Technol A 43(5):2025. http://dx.doi.org/10.1116/6.0004686.

[53] Moysiadou A, Lee S, Hsu C-S, Chen HM, Hu X. Mechanism of oxygen evolution catalyzed by cobalt oxyhydroxide: Cobalt superoxide species as a key intermediate and dioxygen release as a rate-determining step. J Am Chem Soc 2020;142(27):11901–14. http://dx.doi.org/10.1021/jacs.0c04867.

[54] Vazhayil A, Vazhayal L, Thomas J, Ashok C S, Thomas N. A comprehensive review on the recent developments in transition metal-based electrocatalysts for oxygen evolution reaction. Appl Surf Sci Adv 2021;6:100184. http://dx.doi.org/10.1016/j.apsadv.2021.100184.

[55] Pan Q, Wang L. Recent perspectives on the structure and oxygen evolution activity for non-noble metal-based catalysts. J Power Sources 2021;485:229335. http://dx.doi.org/10.1016/j.jpowsour.2020.229335.

[56] Marcks C, Gohlke C, Chatwani M, Jain A, Wagner T, Wöhrl N, Vinayakumar V, Seidl V, Segets D, Mechler AK. Activation of powder-coated electrodes for the alkaline oxygen evolution reaction. Zenodo 2025. http://dx.doi.org/10.5281/zenodo.15212438.